

## 3D Printing of Small and Irregular 316L Powder Through A Novel Slurry-Based LPBF Technique

M. Sinée<sup>1</sup>, M. Sinico<sup>1,2</sup>, S. Meyers<sup>1</sup>, Y. Kinds<sup>1</sup>, and B. Van Hooreweder<sup>1</sup>

<sup>1</sup> Department of Mechanical Engineering, Celestijnenlaan 300, 3001 Leuven, Belgium

<sup>2</sup> Flanders Make@KU Leuven, 3001 Leuven, Belgium

### Abstract

Laser Powder Bed Fusion (LPBF) is a widely adopted additive manufacturing technique for metals. However, due to stringent powder requirements regarding sphericity and flowability, metal powders are typically produced through gas-atomization, of which only a limited size fraction can be used. Enabling the use of small, irregular powders manufactured through water-atomization (WA), milling or from waste streams would greatly reduce LPBF cost and broaden its material palette. In this work, a novel slurry-based LPBF technique was developed in which powder particles are suspended within an aqueous solution. It is used to process WA 316L stainless steel powder with a diameter  $< 20 \mu\text{m}$ , which is a powder batch too irregularly shaped and too small for conventional dry-powder LPBF. Results demonstrate that a wide range of fabrication parameters yield nearly fully dense parts ( $> 99\%$ ). Computed tomography of the dried unscanned slurry cake reveals different populations of defects, providing valuable insights into the drying behavior of the slurry powder bed before the laser fusion step.

### Introduction

Laser Powder Bed Fusion (LPBF) is a well-known Additive Manufacturing (AM) technique that can produce high-quality parts with complex designs at low lead times. Metal or ceramic powders are spread into thin layers on a baseplate, after which a laser fuses the particles together through melting and re-solidification [1]. This step is repeated layer by layer to create the final part. Although LPBF is widely adopted within industry, there remain stringent powder feedstock requirements regarding size and morphology, which impose limitations on the process. Sinico et al. [2] found that it is impossible to form homogeneous powder layers with fine particles fraction (5-15  $\mu\text{m}$ ) of maraging steel due to poor powder flowability and powder agglomeration caused by Van der Waals forces. Spierings et al. [3] observed that the use of fine powder particles results in optimized density and scan surface quality, whereas coarse particles are beneficial for higher elongations at break. However, particle size has to be limited in relation to effective powder layer thickness. Haferkamp et al. [4] concluded that non-spherical water-atomized (WA) 316L powder exhibits insufficient flowability, leading to a lower powder packing density and highly porous parts. Toenjes et al. [5] found that non-spherical WA 410L steel powder requires an 80%-140% increase in volumetric laser energy density (VED) in order to achieve high relative densities, compared to spherical powders. This is mainly attributed to the higher oxidation levels of WA powder, which can cause nanoscale porosities and a reduction in packing density due to the reduced flowability and irregular shape of the powder. It can be concluded that, to ensure good flowability and packing density, the powder feedstock for LPBF needs to be (near)-spherical and fall within a limited particle size range (e.g. 20-60  $\mu\text{m}$ ). Therefore, metal powders are typically produced through gas-atomization, of which only a small fraction of the yield can be used [6]. This

is undesirable from both an economic and ecological point of view, as gas-atomization is expensive and low energy-efficient. Water-atomized powders could be a great alternative for gas-atomized powders as they are significantly cheaper, they are unfit for dry-powder LPBF due to their irregular shape and therefore poor flowability.

To eliminate some of the stringent powder requirements associated with dry-powder LPBF, slurries or colloids can be used as feedstock material. Layer-Wise Slurry Deposition (LSD) [7] is a process where powder particles are suspended within a liquid to form a slurry, which is spread into layers by a recoating mechanism. These slurry layers can be consolidated through multiple routes such as stereolithography [8], binder jetting [9] or Laser Sintering [10]. LSD has already been studied quite extensively for a variety of ceramic metals, including alumina [11] and zirconia [8]. Zocca et al. [12] successfully printed irregularly shaped silicon carbide by sequentially depositing and drying layers of slurry, resulting in a powder bed with high packing density, which was scanned by a laser. However, because a binder is melted and re-solidified and thus used to assist the shaping of the ceramic powder, an additional de-binding step is required before final densification.

Despite multiple research efforts on LSD for ceramics, the research on LSD for metals stays rather limited. Meyers et al. [13] developed a slurry-based LPBF (s-LPBF) technique for metal powders and successfully proved that this technique is suitable for processing small 316L stainless steel powder ( $< 20 \mu\text{m}$ ), resulting in parts with competitive mechanical properties and outstanding surface roughness compared to dry-powder LPBF. During slurry preparation, a binder is added to increase slurry stability, as opposed to ceramic LSD where the binder is needed to assist shaping. Therefore, only very limited amount of binder is used, eliminating the need for an additional de-binding step. However, deeper research into the behavior, processability and opportunities of metal slurries is required.

In this study, a slurry-based LPBF machine was used to test the printability of water-atomized stainless steel powder. Various cuboid samples were printed during a parameter optimization and their processing window was assessed through optical density measurements. This processing window was then compared to that of components from previous work, build with fine gas-atomized 316L powder. Finally, a piece of dried, unscanned slurry cake was examined using micro CT scanning to quantify its internal defects and make a clear distinction between the different types of porosity developed within the powder bed, before the laser fusion step.

### **Slurry-based LPBF machine and process**

Using slurry as feedstock poses certain challenges such as controlled slurry supply, thorough layer drying and in-process coater cleaning. A prototype of a s-LPBF machine is modified to meet these requirements. The inside of the s-LPBF build chamber contains both the slurry supply and deposition subsystem, and the coater and nozzle cleaning subsystem, as depicted in Fig. 1a. The solvent removal and atmosphere control subsystem is located outside the build chamber and is schematically represented in Fig. 1b.

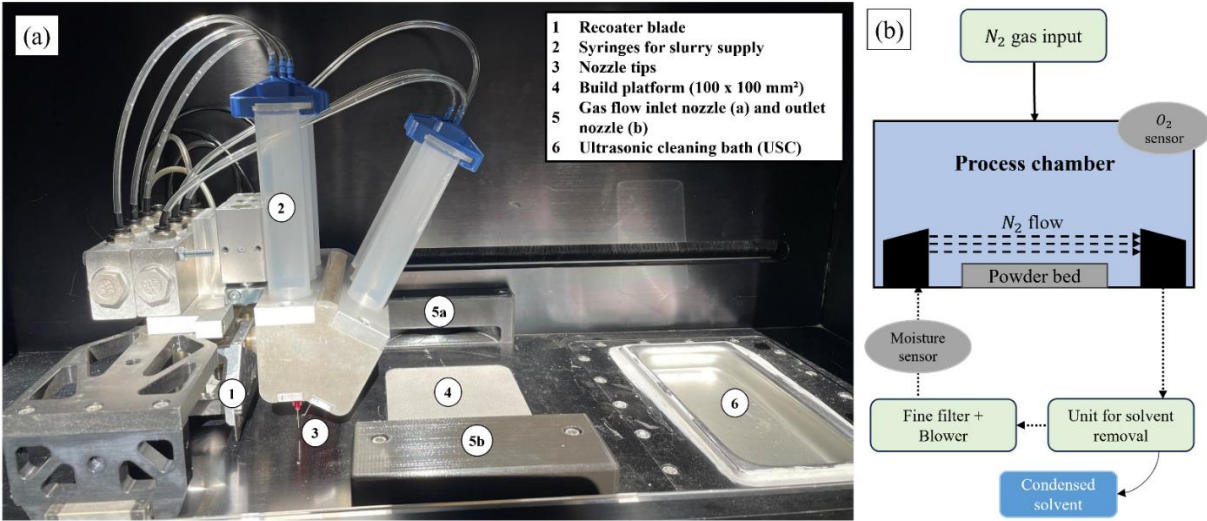


Fig. 1. Overview of the different s-LPBF subsystems with (a) the inside of the build chamber and its components and (b) a schematic overview of the atmosphere control located outside of the build chamber [13].

- Slurry supply and deposition:** The slurry supply and deposition system consists of six 55 cc syringes (2) that are equally spaced within a translating recoater arm. Each syringe is equipped with an interchangeable deposition nozzle tip (3) and internal plunger disk. The slurry deposition quantity and rate are pneumatically controlled by changing deposition time and pressure. The recoater arm is also equipped with a recoater blade (1) that paves a flat layer of slurry onto the build platform (4) in a left-to-right motion.
- Solvent removal and atmosphere control:** The solvent of the slurry is removed by means of a nitrogen gas flow over the powder bed (5a to 5b) that is recirculated through a fine particle filter and brought back into the process chamber. As the solvent evaporates, the moisture level inside the process chamber is constantly increasing. To avoid saturation, a subsystem that removes the solvent from the gas flow is added to the circulation chain. The gas flow is cooled down via thermo-electric cooling elements, causing the solvent to condensate and form droplets that are collected in an external container. Next, the gas flow passes through the fine particle filter and ultimately re-enters the process chamber. Before re-entering, the relative humidity level is measured, guaranteeing that it stays below a given setpoint before scanning the freshly deposited slurry layer. Besides solvent removal, the gas flow also facilitates fume extraction while scanning. During the process, the oxygen levels are continuously monitored by an O<sub>2</sub> sensor, ensuring the oxygen levels stay below 0.2%.
- Coater and nozzle cleaning:** After slurry layer deposition, residual slurry remains attached to the recoater blade and dries. This can cause the formation of stripes on the powder bed during the spreading of subsequent layers. Additionally, small slurry droplets stay attached to the nozzle tips. If not removed, they will dry before reaching the next cycle, obstructing further slurry deposition. To prevent either phenomenon from happening the recoater blade and nozzle tips are pneumatically lowered into an ultrasonic cleaning bath (6) during drying and scanning.

The different subsystems come together to form a slurry-based LPBF machine to print 3D components. The process starts by depositing six equidistant slurry droplets onto the machine plate

using the syringes. The recoater blade lowers and spreads the droplets out into a thin layer of slurry onto the baseplate ( $100 \times 100 \text{ mm}^2$ ). The recoater blade is lowered into the USC for cleaning, during which the slurry is dried by the nitrogen flow. When dried, the powder bed is selectively scanned by a laser. During scanning, the nozzle tips are shortly cleaned within the USC to prevent clogging. After scanning, the blower is stopped and the recoater arm moves to its starting position. This cycle repeats until the desired 3D part is complete. The process cycle is schematically represented in Fig. 2

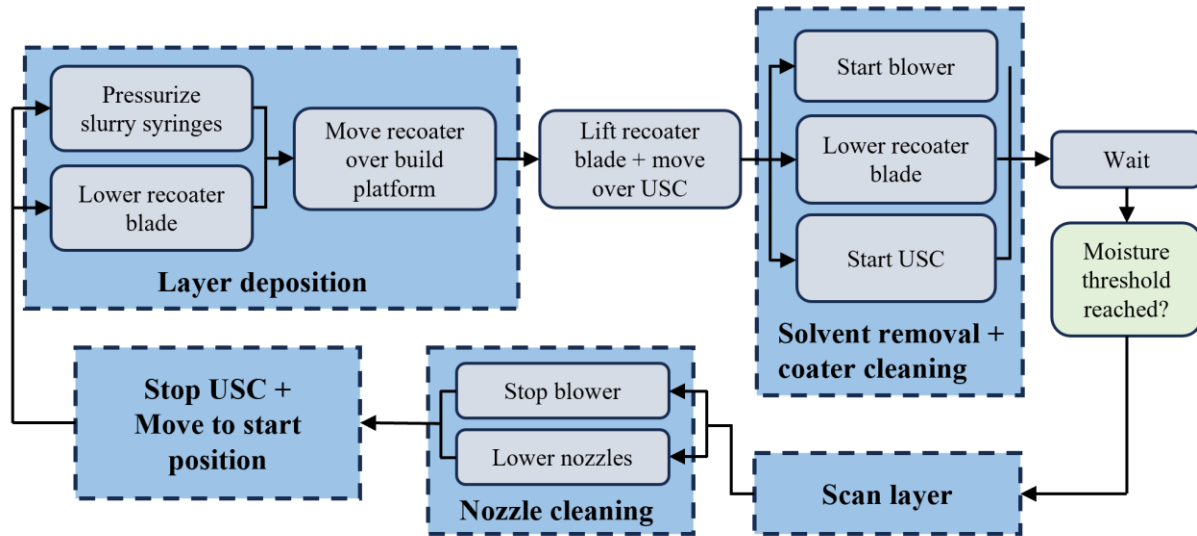


Fig. 2. Schematic overview of the slurry-based LPBF process [13].

## Materials and methodology

### Slurry composition

The feedstock slurry consisted of 40 vol% water-atomized 316L powder (KS Tech,  $d \leq 20 \mu\text{m}$ ) and 60 vol% aqueous solution with a small amount of polymer binder (1 wt%). The reference parts were produced with gas-atomized 316L powder (Höganäs,  $d_{90} \leq 18 \mu\text{m}$ ), with the same powder-to-solvent ratio. The different elements were first mixed by hand, after which they were transferred to a poly-ethylene container and shaken in a Turbula mixer at 75 rpm for 4 h until a homogeneous slurry was obtained.

### Powder and slurry characterization

The powder morphology was assessed using a FEI XL30-FEG scanning electron microscope (SEM) with an accelerating voltage of 10 kV, a spot size of 3 nm and a  $500\times$  magnification. The particle size distribution and median particle size of the powder was obtained using a laser diffraction particle size analyzer (Beckman Coulter LS 13 320).

### s-LPBF process

Slurry-based LPBF was performed using an in-house modified prototype of an Admatec Laserflex Conflux machine. The machine uses a 400 W Trumpf fiber laser with a wavelength of 1063 nm, in continuous wave mode. During process optimization, the laser power  $P$  was varied

from 60-140 W, the scan speed  $v$  was varied from 600-1000 mm/s, with a fixed hatch spacing  $h$  of 60  $\mu\text{m}$ . The 30  $\mu\text{m}$  layers were scanned with a zig-zag strategy with a continuous 67° rotation between successive layers. The WA 316L slurry was deposited through Nordson PTFE coated deposition nozzles with an inner diameter of 0.33 mm and a length of 12.7 mm, with a deposition pressure of 3 bar and a deposition time of 1.75 s. The reference 316L slurry was deposited through a similar deposition nozzle with an inner diameter of 0.25 mm, with a deposition pressure of 3.8 bar and a deposition time of 2.3 s. The drying time was set to 30 s throughout the whole process. All printed parts have dimensions of 10×10×5 mm<sup>3</sup>. For the slurry bed CT analysis, a slurry bed of 70 layers (2.1 mm height) was created. Each layer was deposited and dried, but no scanning was performed.

## **Component characterization**

The printed cuboid samples were embedded (KEM 20, ATM Qness GmbH) and polished using a 0.1  $\mu\text{m}$  diamond suspension. A Keyence VHX-6000 Digital Microscope with 200× magnification was used to record images that cover a 10×4 mm<sup>2</sup> area of the embedded samples. The relative optical density of the cuboids was determined by analyzing the images with an in-house developed MATLAB script. To investigate the internal porosities of the dried slurry cake, before laser fusion, a CT scan was taken from a ~12×9×2.1 mm<sup>3</sup> slurry sample. Specifically, a Nikon XTH 225 ST machine (Nikon Metrology NV, Belgium) was employed with scan settings as follows: 195 kV, 36  $\mu\text{A}$ , 0.25 mm Cu filter, 3142 projections with 1415 ms of exposure time for projection, and an achieved voxel size of 8.7  $\mu\text{m}$ . The reconstruction step was optimized, using a combination of beam hardening, scattering and noise reduction filters to obtain an image stack clear from artefacts. The resulting 3D data was further processed in the software VGSTUDIO MAX 2025.1 (Hexagon AB, Sweden), to perform the porosity/defect analysis using the VGDefX algorithm. The resolution limit for defect detection is estimated to be around 20  $\mu\text{m}$  (circumscribed diameter). The algorithm was run on a limited central volume of ~80 mm<sup>3</sup> to exclude the rough, irregular bottom and side borders, which resulted from sample detachment, from the analysis. The top surface, being the final deposited layer, remained fully intact and also acts as the reference plane to align the sample in the virtual 3D space.

## **Results and discussion**

### **Powder characterization**

To investigate the morphology of both the gas-atomized and water-atomized powder, SEM images were taken. The results (Fig. 3) show that the gas-atomized powder has a near-spherical shape as expected. The water-atomized powder does not only show lower sphericity, but also powder agglomerates. The particle size distribution and median particle size of both the spherical and non-spherical 316L powder were assessed and are visually represented in Fig. 4. The spherical powder has a median particle diameter of 10.26  $\mu\text{m}$ , with a  $d_{10}$  of 4.3  $\mu\text{m}$  and a  $d_{90}$  of 16.9  $\mu\text{m}$ . The non-spherical powder has a mean particle diameter of 12.10  $\mu\text{m}$  with a  $d_{10}$  of 2.5  $\mu\text{m}$  and a  $d_{90}$  of 25.98  $\mu\text{m}$ . This shows that the WA powder has a broader particle size distribution compared to the GA powder. This could lead to a higher packing density during printing, but typically has a detrimental effect on the flowability [14].

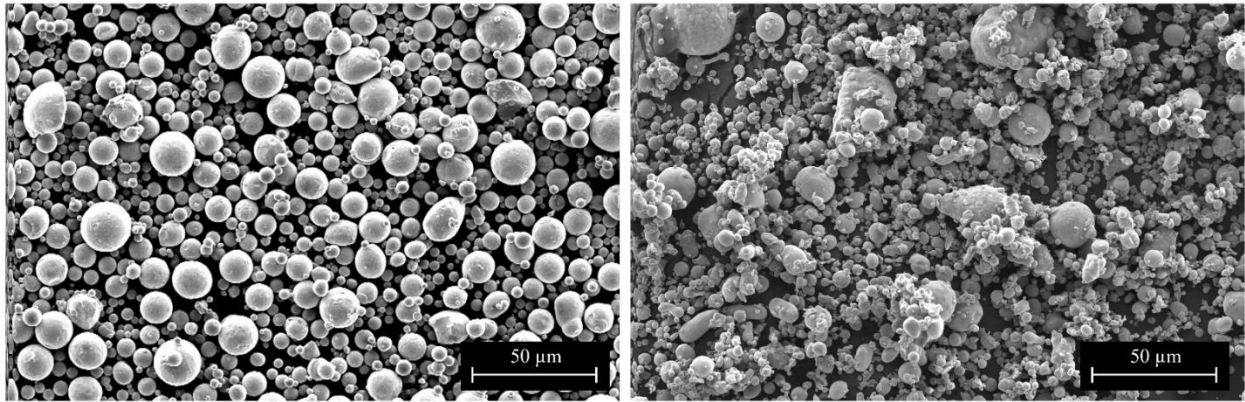


Fig. 3. SEM image of gas-atomized 316L powder (left) and water-atomized 316L powder (right).

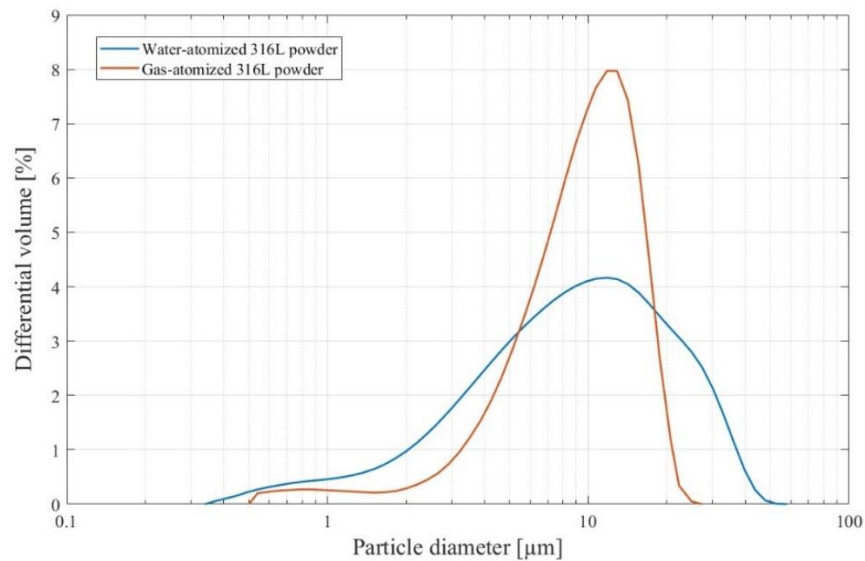


Fig. 4. Particle size distribution of gas-atomized and water-atomized 316L stainless steel powder with a median particle size of respectively 10.26  $\mu\text{m}$  and 12.10  $\mu\text{m}$ .

### Preliminary parameter optimization of water-atomized 316L steel

To assess whether water-atomized 316L powder can be processed through slurry-based LPBF and if so, if a broad processing window is feasible, an initial parameter optimization was performed. Throughout the printing process, the WA slurry showed similar behavior as the spherical 316L slurry [13], having a good flowability and limited spatter formation. A series of 22 cuboids was successfully printed with energy densities ranging between 33.3  $\text{J}/\text{mm}^3$  and 111.1  $\text{J}/\text{mm}^3$ . Their relative optical density  $\rho_{rel}$  was measured and plotted in function of the volumetric laser energy density (VED), as seen in Fig. 5a. It can be observed that the majority of the cuboids have a density above 99%, with a clear trend of increasing relative density with increasing VED, stabilizing towards higher energies. Notably, using high scan speeds has a detrimental effect on the relative density, while lower scan speeds ensure near-full density as can be seen in Fig. 5b.

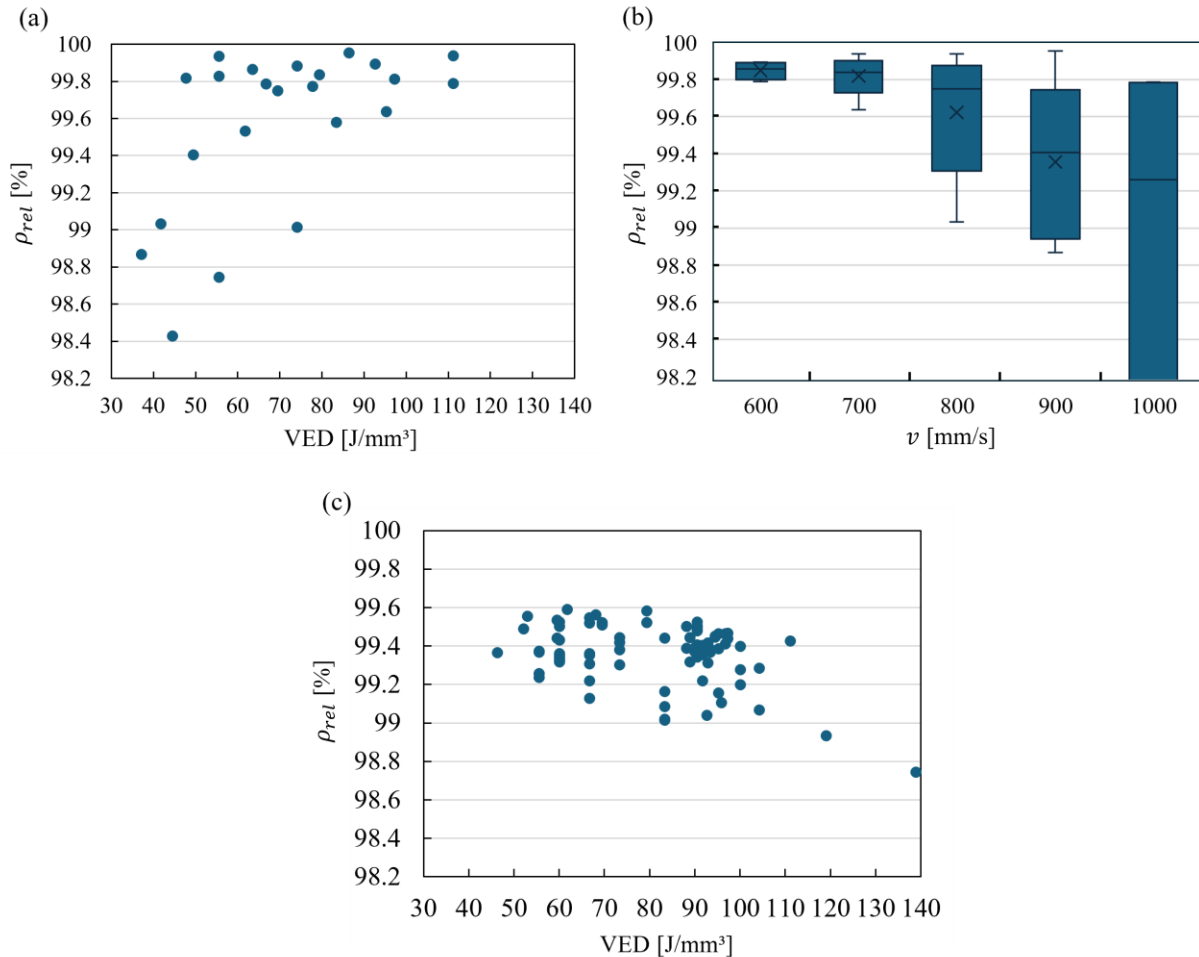


Fig. 5. (a) Measured relative optical density of water-atomized 316L cuboids in function of the volumetric energy density, showing an optimal processing window between 55.6  $J/mm^3$  and (at least) 111.1  $J/mm^3$ , (b) measured relative optical density of water-atomized 316L cuboids in function of the scan speed, indicating that high scan speeds have a detrimental effect on the relative density and (c) measured relative Archimedes density of gas-atomized 316L cuboids in function of volumetric energy density showing a shift in processing window compared to water-atomized 316L samples.

The processing window for WA 316L printed with s-LPBF lies between 55.6  $J/mm^3$  and (at least) 111.1  $J/mm^3$ . It is expected that the processing window will stay stable beyond the highest acquired VED in the experiment, up until keyhole formation or balling [15]. When comparing these results to the reference print job in Fig. 5c [13], a clear shift in the processing window can be observed. The water atomized powder requires a minimum increase of 30% in VED, but shows a broader processing range. The required VED increase is lower than anticipated based on literature [5]. Here, it was seen that the energy increase could be attributed to two factors: lower packing density and oxidation of the powder. For s-LPBF of WA 316L, it is believed that only the higher oxide content plays a role, as the dried slurry bed is expected to have a high powder packing density which results from both the intrinsic characteristics of the process and the irregular morphology and broad particle size distribution of the WA powder.

During the print, two phenomena could be observed. Firstly, the slurry inside the syringes showed sedimentation towards the end of the printing process. This is undesirable as it can lead to variations in the parts across different layers. Moreover, since the duration of the print job was

relatively short, it is anticipated that this effect could become more pronounced in longer prints. Secondly, the drying of the slurry cake showed inconsistent behavior over time. In the first 10-20 layers, drying stayed rather uniform, and the scanned and unscanned areas dried at the same rate. However, as more layers were deposited, the unscanned areas gradually dried faster than the scanned areas. It is believed that capillary forces act upon the freshly deposited slurry, sucking the water towards the baseplate and therefore not allowing sufficient time for it to evaporate. This effect did not occur on previously scanned areas, as there is no path for the water to follow through the dense scanned parts. This uneven drying effect does not pose a problem for the printing of cuboids, but could present an issue when printing overhangs and/or support structures. If the bottom region of the slurry remains moist, the water could evaporate very quickly when scanning with the laser, impacting the surrounding slurry as it expands. More research on why this happens and how to resolve this has yet to be performed.

### **Dried slurry bed analysis**

A small fragment ( $\sim 12 \times 9 \times 2.1 \text{ mm}^3$ ) of the dried unscanned WA slurry cake was taken and subjected to CT inspection to analyze the internal porosity of the powder bed. Due to the  $\sim 20 \text{ }\mu\text{m}$  pore resolution limit of the CT scan, microporosities and most microcracks within the cake remain undetected. The results are presented in Fig. 6, which includes a magnified region indicating the equivalent pore diameter. From this region, three zones can be clearly distinguished. Zone A contains irregular pores, that can be attributed to the removal of the slurry cake during which small dried slurry pieces remain attached to the baseplate, creating cracks and open porosities that might interfere with the subsequent defect analysis. Therefore, this zone, equivalent to the bottom  $\sim 0.25 \text{ mm}$  of the specimen, is excluded for the defects detection and only a total central volume of  $\sim 80 \text{ mm}^3$  is considered. Throughout zone B and C, small pores with an equivalent diameter of  $\pm 0.03 \text{ mm}$  are found. These represent the voids within the powder bed due to the packing arrangement of the powder particles, as they are equally distributed throughout the entire sample. However, due to the already mentioned limited resolution of the CT scan, the true packing density is likely lower than what is captured by this analysis.

Concerning the larger detected defects, for Zone B mainly spherical pores can be observed. On the other hand, starting from a print height of  $0.63 \text{ mm}$ , indicated as zone C, columnar porosities begin to form. Fig. 7 contains a quantitative analysis of the pores in zone B and C, indicating the circumscribed pore diameter in function of their sphericity  $\Psi$ . The porosity content ( $> 20 \text{ }\mu\text{m}$ ) is found to be 2.39%, with an average circumscribed diameter of  $0.07 \text{ mm}$  and an average sphericity of 0.6. The scatter plot reveals two distinct trends in the pore population. First, the columnar pores exhibit low sphericity combined with high circumscribed diameters; as these columns become shorter, their sphericity increases while their circumscribed diameter decreases, consistent with a nearly constant cross-sectional diameter as seen on Fig. 6 and 8. Second, a cluster of pores with lower and similar circumscribed diameters, but with a broader range of sphericity, represents the more equiaxed pores associated with trapped air bubbles and variations in local packing density. Additionally, the partial detection of the microcracks within the dried slurry cake contributes to the population of pores with very low sphericity and low circumscribed diameter, on the bottom left of the graph, with shapes similar to lack of fusion defects as sometimes found in standard LPBF.

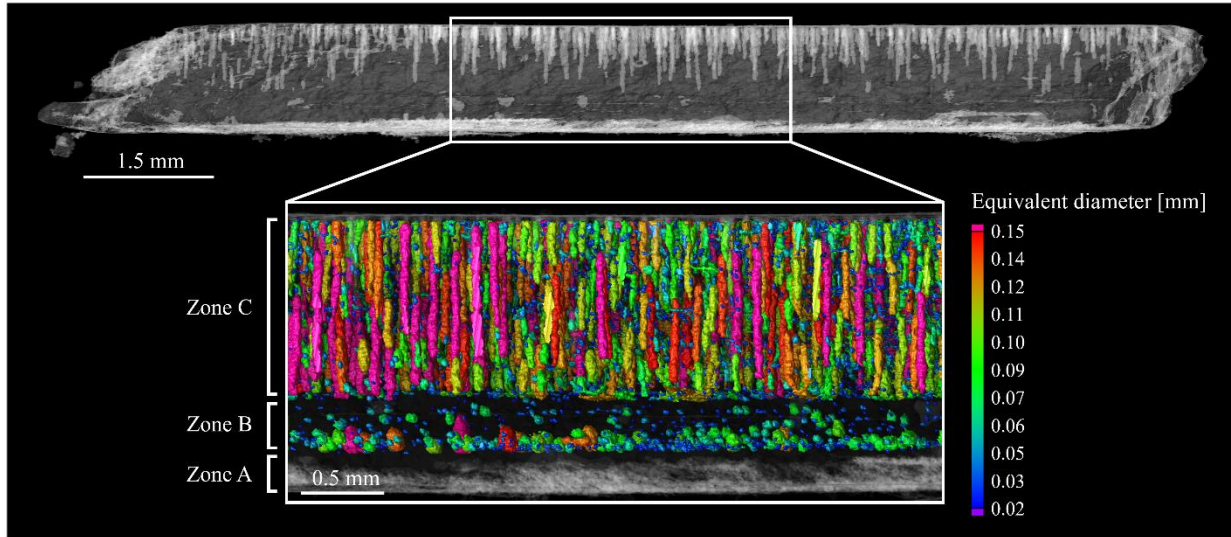


Fig. 6. CT X-ray image of dried unscanned WA slurry cake with a zoomed-in region indicating the equivalent diameter of the internal pores. The region of interest consists of three zones, where Zone B represents manual slurry deposition, and zone C indicates standard machine operation. Zone A indicates slurry cake removal and is omitted from the quantitative analysis.

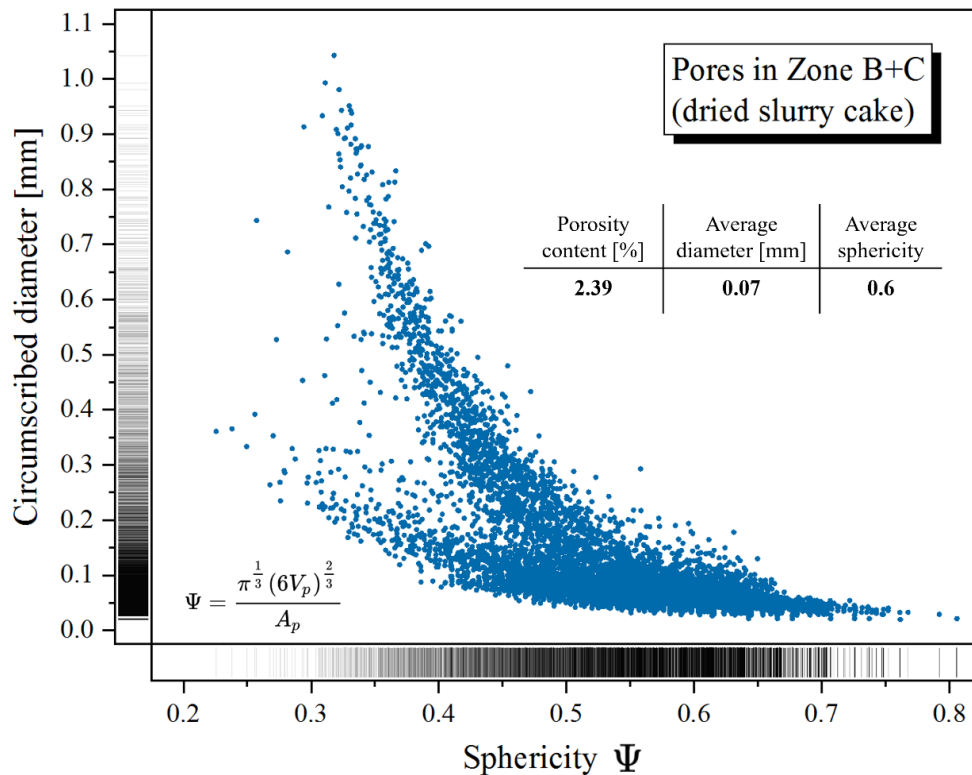
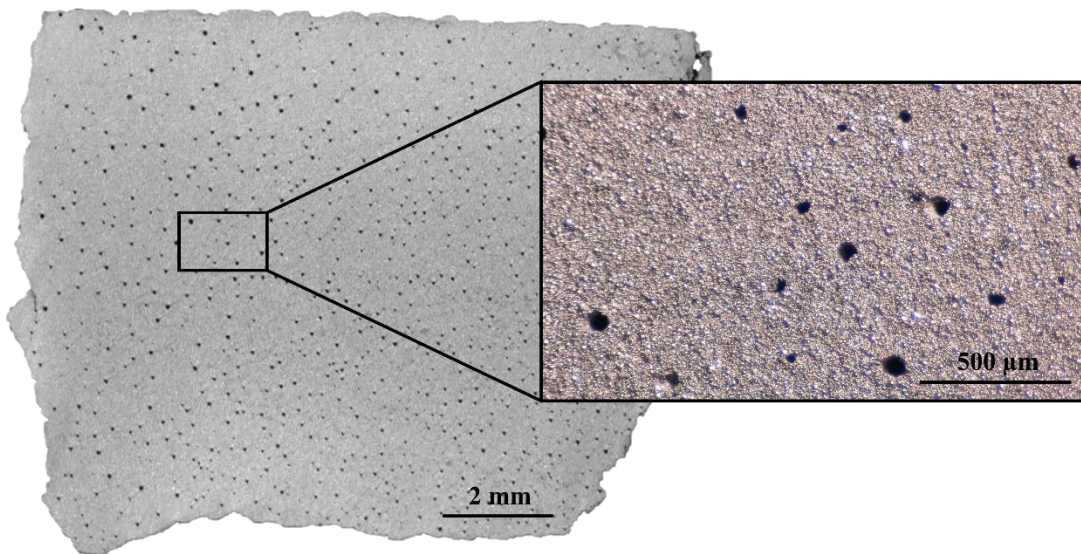


Fig. 7. Quantitative analysis of the pores in zone B and C, for a total volume of  $\sim 80 \text{ mm}^3$ , indicating the circumscribed diameter of the pores in function of their sphericity.

Both the columnar porosities in zone C as well as the larger diameter fraction of porosities in zone B are believed to originate from air bubbles entrapped within the slurry, although they create porosities with different characteristics depending on the processing conditions. In Zone B, a thick layer of slurry was deposited and dried in a single step. As a result, air bubbles became encapsulated within the slurry layer, preventing their escape and therefore resulting in larger

spherical porosities. In contrast, Zone C corresponds to the initiation of continuous operation, during which the slurry is deposited in layers of 30  $\mu\text{m}$  and dried every cycle. Starting from this point, buoyancy forces cause the bubbles to move upwards, creating small holes (Fig. 8) similar to pinhole defects seen in paints and coatings [16]. These pinholes can serve as a preferential site for bubble attachment and growth in subsequent layer deposition, leading to defect propagation throughout the dried powder compact. These columnar channels could attribute to the uneven drying rate between scanned and unscanned areas, as water can readily flow through them towards the baseplate. Additionally, a change in powder bed density can influence the thermal history of the part, since regions with higher porosity exhibit lower thermal conductivity and higher local laser absorption, resulting in slower heat dissipation and altered melt pool dynamics [17]. This can lead to local variations in cooling rates, melt pool shape, and solidification behavior throughout the build height.



*Fig. 8. CT image of the top surface of the dried unscanned slurry cake, with a more detailed microscopic image showing the small holes similar to pinhole defects in paints and coatings.*

Further research is needed to investigate the potential correlation between the defects observed in the dried, deposited slurry cake and the porosity content in the final metal parts. Optimization of the slurry formulation and drying process should also be explored to enhance the powder bed packing density and reduce the formation of pinhole defects. Nevertheless, the high relative density achieved in the fused metal parts (Fig. 5) suggests that many of the initial defects in the dried slurry may not significantly influence the final part quality. This indicates a degree of defect tolerance in the process, where the laser fusion step effectively mitigates or eliminates some of the pre-existing porosities in the slurry powder bed, resulting in parts with acceptable or even excellent density and integrity. The last statement is only valid, at this stage, for simple geometries and should be further checked in the case of parts with e.g. overhangs, thin walls, or complex lattices.

## **Conclusions**

Slurry-LPBF is a novel 3D printing technique where powder particles are dispersed in a liquid medium, deposited layer by layer, dried and subsequently consolidated by a laser. This technique offers a promising alternative to conventional dry-powder LPBF as it has the potential to eliminate its stringent powder requirements regarding particle size and morphology. Previous studies have proven that s-LPBF is a viable route for printing small gas-atomized powder particles, with good mechanical properties and outstanding surface roughness. In this work, the feasibility of using irregular water-atomized 316L powder as a feedstock material for s-LPBF was assessed, and the processing window and powder bed quality were determined and discussed in detail.

The processing window for WA 316L stainless steel powder on the s-LPBF system was established through a parameter optimization. Results indicate that a relatively wide range of VED can yield near-full density components. However, the minimum VED required for stable processing is notably higher than that of gas-atomized 316L, though still lower than what prior studies would suggest. A clear correlation was identified between scan speed and relative density, with increased scan speeds leading to reduced part density.

Finally, a computed tomography analysis of a dried, unscanned slurry layer revealed distinct porosity patterns within the slurry powder bed. An initial zone of larger, spherical pores indicates the entrapment of air bubbles during machine start-up, whereas columnar pores were formed during continuous operation. As gas bubbles escape from the deposited layer, pinhole defects were created and act as a preferential site for bubble attachment and growth in subsequent layer deposition, leading to defect propagation throughout the dried powder compact. Future studies should explore degassing strategies to minimize bubble formation and clarify its role in slurry bed behavior, while also investigating the link between dried layer defects and final part porosity, especially for complex geometries.

Overall, this study broadens the material palette for LPBF by demonstrating the feasibility of using cost-effective, irregularly shaped powders in s-LPBF, representing a step toward more sustainable routes for additive manufacturing of metals.

## **Acknowledgements**

This work was financially supported by KIC RawMaterials under project HiPAM. KIC RawMaterials is supported by the European Institute of Innovations and Technology, a body of the European union. The authors would like to acknowledge the Computed Tomography Lab – Department of Mechanical Engineering, part of the KU Leuven XCT Core Facility (kuleuven.xct.be). Lastly, the authors would like to thank Kopila Gurung for contributing to the proof-of-concept stage of this research.

## **References**

- [1] J.-P. Kruth, G. Levy, F. Klocke and T. Childs, "Consolidation phenomena in laser and powder-bed based layered manufacturing," *CIRP Annals*, vol. 56, no. 2, pp. 730-759, 2007, <https://doi.org/10.1016/j.cirp.2007.10.004>.

- [2] M. Sinico, A. Witvrouw and W. Dewulf, "Improving the surface quality of maraging 300 parts produced via laser powder bed fusion through powder distribution selection and optimized laser remelting," *Journal of Manufacturing Processes*, vol. 138, pp. 38-49, 2025, <https://doi.org/10.1016/j.jmapro.2025.02.014>.
- [3] A. Spierings, N. Herres and G. Levy, "Influence of the particle size distribution on surface quality and mechanical properties in AM steel parts," *Rapid Prototyping Journal*, vol. 17, no. 3, pp. 195-202, 2011, <https://doi.org/10.1108/13552541111124770>.
- [4] L. Haferkamp, L. Haudenschild, A. Spierings, K. Wegener, K. Riener, S. Ziegelmeier and G. J. Liechtfried, "The Influence of Particle Shape, Powder Flowability, and Powder Layer Density on Part Density in Laser Powder Bed Fusion," *Metals*, vol. 11, no. 3, p. 418, 2021, <https://doi.org/10.3390/met11030418>.
- [5] A. Toenjes, J. Schmidt and M. Hesselmann, "Processability of water atomized 310L steel with laser powder bed fusion," *Progress in Additive Manufacturing*, 2025, <https://doi.org/10.1007/s40964-025-00979-9>.
- [6] O. K. Radchenko and K. O. Gogaev, "Requirement for Metal and Alloy Powders for 3D Printing (Review)," *Powder Metallurgy and Metal Ceramics*, vol. 61, pp. 135-154, 2022, <https://doi.org/10.1007/s11106-022-00301-0>.
- [7] A. Gahler, J. Heinrich and J. Günster, "Direct Laser Sintering of Al<sub>2</sub>O<sub>3</sub>-SiO<sub>2</sub> Dental Ceramic Components by Layer-Wise Slurry Deposition," *Journal of the American Ceramic Society*, vol. 89, pp. 3076-3080, 2006, <https://doi.org/10.1111/j.1551-2916.2006.01217.x>.
- [8] Y. Jiao, G. Ye, J. Sun, W. Yu, F. Gong, P. Zhou, J. Bai, M. Yan and G. Liu, "A comprehensive study on zirconia slurry for stereolithography-based additive manufacturing," *Journal of Sol-Gel Science and Technology*, vol. 105, pp. 827-835, 2023, <https://doi.org/10.1016/j.addma.2021.101994>.
- [9] P. Lima, A. Zocca, W. Acchar and J. Günster, "3D printing of porcelain by layerwise slurry deposition," *Journal of the European Ceramic Society*, vol. 38, no. 9, pp. 3395-3400, 2018, <https://doi.org/10.1016/j.jeurceramsoc.2018.03.014>.
- [10] T. Mühler, J. Heinrich, C. M. Gomes and J. Günster, "Slurry-Based Additive Manufacturing of Ceramics," *International Journal of Applied Ceramic Technology*, vol. 12, no. 1, pp. 18-25, 2015, <https://doi.org/10.1016/j.jeurceramsoc.2014.10.019>.
- [11] A. Zocca, P. Lima and J. Günster, "LSD-based 3D printing of alumina ceramics," *Journal of Ceramic Science and Technology*, vol. 8, no. 1, pp. 141-148, 2017, <https://doi.org/10.4416/JCST2016-00103>.
- [12] A. Zocca, P. Lima, S. Diener, N. Katsikis and J. Günster, "Additive manufacturing of SiSiC by layerwise slurry deposition and binder jetting (LSD-print)," *Journal of the European Ceramic Society*, vol. 39, no. 13, pp. 3527-3533, 2019, <https://doi.org/10.1016/j.jeurceramsoc.2019.05.009>.
- [13] S. Meyers, K. Gurung, Y. Kinds and B. V. Hooreweder, "On the use of slurry as an alternative to dry powder for laser powder bed fusion of 316L stainless steel," *Additive Manufacturing Letters*, vol. 11, 2024, <https://doi.org/10.1016/j.addlet.2024.100230>.
- [14] S. E. Brika, M. Letenneur, C. A. Dion and V. Brailovski, "Influence of particle morphology and size distribution on the powder flowability and laser powder bed fusion manufacturability of Ti-6Al-4V alloy," *Additive Manufacturing*, vol. 13, 2020, <https://doi.org/10.1016/j.addma.2019.100929>.

- [15] N. Ahmed, I. Barsoum, G. Haidemenopoulos and R. K. A. Al-Rub, "Process parameter selection and optimization of laser powder bed fusion for 316L stainless steel: A review," *Journal of Manufacturing Processes*, vol. 75, pp. 415-434, 2022, <https://doi.org/10.1016/j.jmapro.2021.12.064>.
- [16] C. K. Schoff, "Craters and Other Coatings Defects: Mechanisms and Analysis," in *Protective Coatings: Film Formation and Properties*, Springer Cham, 2017, pp. 403-425, [https://doi.org/10.1007/978-3-319-51627-1\\_18](https://doi.org/10.1007/978-3-319-51627-1_18).
- [17] P. Wei, Z. Wei, Z. Chen, J. Du, Y. He and J. Li, "Fundamentals of radiation heat transfer in AlSi10Mg powder bed during selective laser melting," *Rapid Prototyping Journal*, vol. 25, no. 9, pp. 1506-1515, 2019, <https://doi.org/10.1108/RPJ-11-2016-0189>.